

# Spectroscopic Imaging Ellipsometry of Self-Assembled SiGe/Si Nanostructures

M. I. Alonso <sup>a,\*</sup>, S. Funke <sup>b</sup>, A. González <sup>b</sup>, M. Garriga <sup>a</sup>,  
P. O. Vaccaro <sup>a,c</sup>, A. R. Goñi <sup>a,c</sup>, A. Ruiz <sup>d</sup>, M. Alonso <sup>d</sup>, and  
P. H. Thiesen <sup>b</sup>

<sup>a</sup>*Institut de Ciència de Materials de Barcelona, ICMA-B-CSIC, Campus de la  
UAB, 08193 Bellaterra, Spain*

<sup>b</sup>*Accurion GmbH, Stresemannstraße 30, 37079 Göttingen, Germany*

<sup>c</sup>*ICREA, Passeig Lluís Companys 23, 08010 Barcelona, Spain*

<sup>d</sup>*Instituto de Ciencia de Materiales de Madrid (ICMM-CSIC), Sor Juana Inés de  
la Cruz 3, Cantoblanco, 28049 Madrid, Spain*

---

## Abstract

Spectroscopic imaging ellipsometry is used to characterize films containing self-assembled SiGe/Si in-plane nanowires grown by Molecular Beam Epitaxy on a Si (001) substrate. The spatial resolution of the order of  $\sim 1 \mu\text{m}$  allows to study individual nanowires. The obtained images consist of both  $\psi$  and  $\Delta$  values measured in every pixel. From them, spatially resolved contributions to the dielectric function within the films are well visible, coming for example from composition variations. In particular, a strong in-plane anisotropy of the optical response of the nanowires is evidenced. Spectroscopic measurements from different regions of the film are analyzed and compared to spectra calculated using standard ellipsometry multilayer models. The results show the potential of imaging ellipsometry to study micro- and

nanostructured semiconductor samples.

*Key words:* spectroscopic imaging ellipsometry, in-plane nanowires, dielectric function, silicon-germanium alloys, anisotropic absorption

---

## 1 Introduction

Spectroscopic ellipsometry is a non-invasive and powerful technique to investigate both structural and optical properties of materials [1,2]. It is very well suited for semiconductor systems, in which it is not only applied in research but also at mass-production scales [3]. Typically, film thicknesses and/or optical constants of multilayer structures employed in microelectronic fabrication processes are determined [4]. However, technological advances towards micro- and nano-structured samples increasingly require spatial resolution as key capability. One possibility is ellipsometric mapping with a focused spot of tenths of  $\mu\text{m}$  [5]. Even for samples where this resolution is sufficient, the angular spread of the incident light beam introduces some depolarization, and the scanning process may be relatively slow. Therefore, imaging ellipsometry has been in continuous development to improve both lateral resolution, measurement accuracy, and time of image acquisition. State-of-the-art imaging systems use a collimated light beam and the light reflected from the illuminated sample area is collected by a high numerical aperture microscope objective and imaged onto a 2-dimensional detector array [6]. The pixel size is chosen such that the lateral resolution is only limited by the optical system. In this way, imaging ellipsometry combines the accuracy of conventional ellipsometry with the

---

\* Corresponding author. Fax: + 34 935 805 729  
*Email address:* `isabel@icmab.es` (M. I. Alonso).

lateral resolution typical of optical microscopy, such that the optical functions of microstructures can be readily investigated.

In this work, we study films containing self-assembled SiGe/Si in-plane nanowires (NWs) grown by Molecular Beam Epitaxy (MBE) on Si (001) substrates. Silicon-Germanium epitaxial nanostructures on Si (001)-oriented wafers are compatible with standard microfabrication technology and therefore useful for integration into the silicon platform. In particular, type IV semiconductor NWs are among the most interesting morphologies for integrated photonic devices [7,8]. We have studied the formation of in-plane, unconventional SiGe epitaxial NWs by MBE on Si (001) substrates by using AuSi seeds obtained by annealing Au layers deposited on clean Si surfaces. We have found suitable conditions of the vapor-liquid-solid process to obtain homogeneous growth of in-plane NWs not mixed with other nanostructure geometries [9], with NWs oriented along the  $\langle 110 \rangle$  directions on the substrate surface. The planar geometry is the most convenient architecture to integrate NW functionalities into microfabricated devices [10]. We perform ellipsometric measurements to characterize the optical properties of the grown films. In a previous study of similar samples by Raman imaging [11], we observed differences in Raman scattering intensity when the light polarization was parallel or perpendicular to the NW axis. Quantitative evaluation showed that the origin of these variations was probably related to anisotropic absorption in the nanowires whereas the intrinsic Raman efficiency seemed less affected by the nanostructure geometry. In this work, we show that the optical response of individual NWs can be studied within the spatial resolution of the imaging ellipsometry system and find striking anisotropic optical properties.

## 2 Experimental details

The studied sample was grown as previously described in detail [9]. Succinctly, a clean Si (001) substrate was introduced in an MBE system where a flat 200 nm-thick c-Si buffer layer was grown at a substrate temperature of 750°C. After cooling the substrate to about 100°C, a bilayer consisting of 1 nm of Au and 1 nm of a-Si was deposited. Liquid SiAu droplets were obtained by thermal annealing at 800°C for 5 minutes. The substrate temperature was then quickly lowered to 550°C and SiGe NWs were obtained by continuous supply of a Ge flux while the substrate was rotated to ensure an homogeneous deposition. The total deposited Ge quantity was equivalent to a planar film thickness of 24 nm, as estimated from the pre-calibrated Ge flux and growth time. For such a large deposited amount of Ge, there was a coalesced film or wetting layer growth among the NWs. We used a shadow mask to leave an undeposited reference region and imaged the region near the shadow border, where both substrate and film regions can be compared. Due to the shadowing effect, the effectively deposited Ge quantity near the border was smaller than the nominal value of 24 nm [11].

Both conventional and imaging ellipsometry data were acquired. "Macroscopic" ellipsometric spectra (SE) of  $\tan \psi$  and  $\cos \Delta$  were measured with a Sopralab GES5E rotating polarizer ellipsometer with a focused spot size of  $\sim 100 \mu\text{m}$ . The spectral bandwidth in the visible was approximately 10 meV. Microscopic images (SIE) were gathered using the Accurion EP4 instrument operating on the principle of classical nulling ellipsometry. In this case, the incident laser beam was elliptically polarized after it passed through a linear polarizer (P) and a quarter-wave compensator plate (C). The elliptically

polarized light was then reflected off the sample (S) and some part (field of view) collected through a long working distance objective ( $50\times$ ,  $NA=0.45$ ), passed through an analyzer (A), and was imaged onto a CCD camera, providing an image of the field of view. In this PCSA configuration, combination of two null conditions (2 zones) at each image pixel allowed to obtain accurate spectroscopic ellipsometry maps in which every pixel depicted a measured  $\psi$  or  $\Delta$  value [4] with minimum systematic errors. These maps provided high contrast of the sample with lateral resolution close to the diffraction limit of the illuminating light, depending on its wavelength, that is, of the order of  $\sim 1\ \mu\text{m}$  in the visible. The spectral bandwidth in this case was approximately 25 meV in the visible.

### 3 Microscopic images

The resolvable feature size  $d$  using an optical microscope is estimated from the Abbe diffraction limit [12] according to:

$$d = \frac{1.22\ \lambda}{2n \sin \theta} = \frac{1.22\ \lambda}{2NA} \quad , \quad (1)$$

where  $\lambda$  is the wavelength of light and  $NA$  the numerical aperture of the objective lens given by the half-angle  $\theta$  subtended by it and the index of refraction  $n$  of the medium. In the best case  $NA \approx 1$  and the smallest resolvable features are roughly half the used wavelength. The value  $d$  also gives the width of the central Airy diffraction maximum [12] which contains most of the reflected light intensity. The typical lateral dimensions of the NWs investigated in this work are smaller than the achievable  $d$ . Since the liquid SiAu seeds are formed by annealing, there is a distribution of lateral sizes. Typical morphologies ex-

tracted from AFM profiles [9,11] are characterized by a top facet of about 100 nm width in all cases, although the total width including the lateral facets can range between 100 and 500 nm. In the optical images these dimensions appear larger (ca. 800 nm) and alike for all NWs because they are affected by the diffraction limit. However, the density of nanostructures on the film surface is relatively low and optical microscopy can resolve them individually. Even if the optical images do not show the real lateral dimensions of the NWs, most of the reflected light intensity by each NW is in the central Airy maximum. As self-normalized measurement, no absolute intensity measurements are needed in ellipsometry, and measured  $\psi$  and  $\Delta$  values at the central pixels are mainly given by the NW optical properties.

Figure 1 shows (a) an optical micrograph and (b) an ellipsometric contrast micrograph of similar areas near the shadow border as described in Section 2. The optical image was obtained with an Optika microscope with a 100 $\times$ , NA=0.90 objective and polarized light. Many details are observed in the optical micrograph but the NWs are particularly difficult to see. We could detect them by illuminating with light polarized along their axis, as shown in Fig.1(a). Many more morphological details are observable in the ellipsometric contrast micrograph, Fig.1(b), where the contrast due to topographic features can be improved by changing the polarizer-compensator-analyzer (PCA) settings. For comparison, Fig. 1(c) shows a scanning-electron microscope (SEM) image acquired using a Quanta-200 ESEM-FEG from FEI, composed by secondary and back-scattered electrons, to obtain the optimum contrast due to both topography and composition. This means that, in general, darker (brighter) regions are both at lower (higher) level and composed by lighter (heavier) elements, respectively. According to this, the darker parts are Si and the brighter ones

contain Ge. Au-rich clusters are also clearly visible in the upper part of the SEM image.

Ellipsometric contrast micrographs provide rather clear images of the film, much improved in comparison to just optical microscopy with polarized light as displayed in Figs.1(a) and (b). In addition, the ellipsometric setup allows to measure maps of ellipsometric parameters. Figure 2 shows the  $\psi$  and  $\Delta$  images over the same full focused sample region of  $100\text{ }\mu\text{m}\times 100\text{ }\mu\text{m}$  shown in Fig.1(b). For an angle of incidence of  $\varphi = 40\text{ deg}$  the field of view is approximately square. The nanostructures are clearly observed as elongated needles of  $\sim 5\text{ }\mu\text{m}$  length. In this case, the contrast in  $\psi$  and  $\Delta$  maps is primarily given by the different optical properties of the film components. Although both  $[110]$  and  $[1\bar{1}0]$  oriented NWs can be distinguished, those which are aligned with the plane of incidence of light (vertical in the image) are accentuated with respect to those which are perpendicularly oriented to it. Comparing Fig. 2 to Fig.1(b) in which morphology was the main contrast factor, it is obvious that the in-plane optical response of the NWs is quite anisotropic. Furthermore, the compositional inhomogeneity present on the sample surface is well visible from the different  $\psi$  and  $\Delta$  values observed at the images. The optical properties of the sample can be extracted from the ellipsometric measurements and therefore, ellipsometry imaging provides compositional sensitivity in addition to the improved polarization microscopy tool. In order to achieve a more quantitative evaluation of sample parameters, spectroscopic maps have also been measured and analyzed. The results are presented in the next Section.

## 4 Spectroscopic results

In the previous section, the shown ellipsometric images were measured at the single wavelength of 430 nm (2.88 eV). In order to take advantage of ellipsometry for characterization of the composition of the studied film, images at other various wavelengths in the range from 400 to 520 nm (3.10 to 2.38 eV) were acquired. A summary of these measurements is given in Fig. 3, where different spectral behaviors have been identified by a "flake search" routine which is described in greater detail in Ref. [13]. In the flake search, every pixel of the spectroscopic  $\psi$  and  $\Delta$  maps is compared to reference values at a given point in the spectra. Every pixel that is in the defined  $\pm \psi$  and  $\Delta$  range, is called a pixel in range. If the relative number of pixels in range to measured spectral points is above a defined threshold, these pixels will be marked with a common color. The different colors depicted in Fig. 3(a) correspond to the  $\psi$  and  $\Delta$  spectra plotted as Figs. 3(b) and (c), respectively. They identify zones of the imaged region with similar optical properties. The largest observed differences are found between the pixels that correspond to NWs aligned with the plane of incidence of light (vertical in the images) and the rest, where the differences are smaller and less significant.

Spectroscopic ellipsometry has been previously used to characterize films with SiGe nanostructures, see f. i. Ref. [14]. However, the sample investigated in this work has obvious compositional inhomogeneities that cannot be suitably identified from average conventional SE spectra. For example, the pronounced absorption anisotropy of the NWs is not detectable from an average spectrum from the film.



In the following, we are going to consider different sets of spectroscopic data measured by SE or SIE and compare them to each other as well as to simulations based on standard multilayer and effective medium models. Instead of plotting the  $\psi$  and  $\Delta$  spectra (or  $\tan \psi$  and  $\cos \Delta$ ), we plot the experimental data as pseudodielectric functions by using the analytic relationship:

$$\langle \varepsilon \rangle = \left( \frac{1 - \rho}{1 + \rho} \right)^2 \tan^2 \varphi \sin^2 \varphi + \sin^2 \varphi, \quad (2)$$

where  $\rho = \tan \psi \exp i\Delta$  is the measured complex reflectance ratio and  $\varphi$  the angle of incidence. Equation 2 only yields true dielectric functions in the isotropic two-phase 1-ambient/2-sample case. Nevertheless, in many cases it offers a physically intuitive picture. Here, this representation is useful to compare the different sets of data taken at different angles of incidence and to visualize the changes in the actual dielectric functions of the different film regions. Simulations and fitting procedures are also run on  $\langle \varepsilon \rangle$  spectra.

We start by considering the substrate region. Some spectra from this region are displayed in Fig. 4(a). There are several details to notice. First, we observe an oscillatory behavior of the spectra in the low absorption region of Si, both in the SE and the SIE spectra. The positions of these oscillations are the same in both measurements although the measured absolute values do not coincide. The SE spectra cover a broader energy range and they show the well-known  $E_1$  and  $E_2$  interband electronic transitions from Si near 3.4 and 4.3 eV respectively [15]. The rather low value of the imaginary part  $\langle \varepsilon_2 \rangle$  at the  $E_2$  peak is indicative of the presence of overlayers (like roughness or oxide) [1,4,15]. The most plausible explanation of the difference in absolute values between SE and SIE is that the effect of overlayers is more pronounced in the former than in the latter case. Indeed, the SE spectra probe a larger substrate region includ-

ing SiAu clusters and therefore they contain various contributions whereas the SIE spectrum of Fig. 4(a) only represents the Si surface. Accordingly, the differences can be quantified by comparison with a suitable model. To account also for the observed oscillations, which agree with the grown 200 nm-thick c-Si buffer layer, we had to assume that an unknown metallic layer was on the initial substrate surface. This metallic contamination layer was actually confirmed by cross section transmission electron microscopy (TEM) in a similar sample, shown as inset in Fig. 4(a). Comprehensive TEM investigations of the NWs will be presented elsewhere [16]. The model that is plotted as calculated curves in Fig. 4(a) is in general a 5-phase model consisting of 1-ambient/2-EMA(Au+SiO<sub>2</sub>)/3-c-Si/4-metallic layer/5-substrate (c-Si). Layer number 4 was simulated by a Drude function fitted to parameters  $E_p = 3.3126$  eV and  $\Gamma = 0.067$  eV and thickness of 0.16 nm. The c-Si buffer layer, layer number 3, is fitted to be 203 nm thick. Layer number 2 is different in the different cases. For the SIE spectrum of Fig. 4(a) the layer number 2 in the stack is just a 5.4 nm thick SiO<sub>2</sub> layer because the selected pixels do not contain AuSi clusters. The obtained oxide thickness of 5.4 nm is relatively large, however, note that in this fit we cannot distinguish oxide from roughness. For the SE spectra, the only way of getting a satisfactory fit is to include the Au contribution by an EMA as already mentioned: the overlayer is fitted as 8.5 nm thick and its composition (0.9 SiO<sub>2</sub> + 0.1 Au), taking as Au reference spectrum literature data [17]. The SIE spectra measured in gold rich regions, i.e., the  $\psi$  and  $\Delta$  spectra plotted in Figs. 3(b) and (c) can be approximated with a similar model in which the Au contribution is more prominent. In that case layer 2 is represented by an EMA layer composed by (0.4 c-Si + 0.6 Au). Hence, the ellipsometric measurements provide qualitative compositional sensitivity.

Considering now the deposited part, the situation is similar to that of the substrate but more complex. The SE spectrum shown in Fig. 4(b) contains mixed contributions from coalesced film regions and from different NWs. The pseudodielectric function that corresponds to the SE measurement is similar to that of the substrate but with broader  $E_1$  and  $E_2$  interband electronic transitions. Due to the mixed contributions, a fit with a multilayer model for the deposited part has too large uncertainties in order to be able to determine, for instance, the average thickness of the deposited film. The oscillations mainly due to the buffer layer thickness are still visible in the region of low absorption. However, the more prominent structure near 3 eV is originated in the deposited SiGe material and corresponds to the  $E_1$  critical point. Its energy position in the SE measured  $\langle \varepsilon \rangle$  in Fig. 4(b) is clearly redshifted with respect to that of the Si substrate in Fig. 4(a). This energy position can be used to obtain information about the composition of the deposited material. In  $\text{Si}_{1-x}\text{Ge}_x$  alloys the  $E_1$  energy and the spin-orbit splitting  $\Delta_1$ , measured in eV, depend on  $x$  as [15]

$$\begin{aligned} E_1(x) &= 3.395 - 1.287x - 0.153x(1-x), \\ \Delta_1(x) &= 0.033 + 0.155x + 0.091x(1-x). \end{aligned}$$

(3)

The energy of the  $E_1$  transition in the SE measurement shown in Fig. 4(b) indicates a Ge content  $x \approx 0.3$  which is compatible with previous evaluations using Raman scattering [11]. The small value of  $\Delta_1 \approx 0.1$  that corresponds to this composition according to Eq. (3) cannot be resolved in the measurement, in part because of the large broadening of the experimentally observed structure resulting from the average of several contributions. These contributions

can be discerned in the SIE measurements compared in Fig. 4(b), where the energy positions of the  $E_1$  structure in spectra averaged over different surface areas of the film differ. The SIE measurements in small coalesced film areas indicate a larger red shift of the  $E_1$  transition compared to a large-area average. Evaluating the corresponding film composition with help of Eq. (3) we find that the Ge content in the coalesced film areas among the NWs is  $x \approx 0.4$ .

It is clear that an average measurement of this film such as the SE curve of Fig. 4(b) should contain all contributions existent in the film. However, the very different values that correspond to the NWs parallel to the plane of incidence (identified as "vertical" in Fig. 3) are imperceptible in the average, as is also demonstrated by considering all SIE contributions over a large area (SIE-averaged curve of Fig. 4(b)). Therefore, only from the spatially resolved SIE measurements it is possible to investigate the optical response of the NWs, which display a strong in-plane anisotropy. Since the distribution of NWs in  $[110]$  and  $[1\bar{1}0]$  directions is statistically the same and the ellipsometric values measured for most NWs are comparable, we can consider that the obtained pseudodielectric functions in vertical or horizontal orientation in the images are representative for the observed NW anisotropy. This is based on the first-order approximation worked out by Aspnes [18] according to which the components of the dielectric tensor of a biaxial crystal are related to pseudodielectric functions calculated in the isotropic two-phase model from ellipsometric data as given by Eq. (2). If  $\varepsilon > 1$  and one of the principal axes is normal to the plane of incidence, the dominant contribution is shown to arise from the projection of the dielectric tensor onto the line of intersection between surface and plane of incidence. In our particular case, the anisotropic in-plane components of the NWs dielectric tensor can be approximated by the

pseudodielectric functions calculated from the measurements with the plane of incidence parallel or perpendicular to the orientations of the NWs, because two principal axes of the tensor should be in-plane, given by the NW geometry.

Figure 5 displays an overview of results to illustrate the large observed anisotropy. In the lower part of Fig. 5, two representative spectra measured in the two configurations of the plane of incidence are plotted as the complex pseudo-(refractive index) given by  $\sqrt{\varepsilon}$  (Eq. (2)). These spectra are calculated only from the values of few pixels selected on one NW each, with the two possible orientations. For comparison, the spectrum of a  $\text{Si}_{0.7}\text{Ge}_{0.3}$  alloy is also plotted. This spectrum is derived from the data of Ref. [15] using a parameterized model to interpolate between experimentally measured compositions. The component along the NWs shows very large values in the measured spectral range, in particular an extremely strong feature appears at 2.54 eV. This feature can be described by a Lorentzian oscillator with a narrow width of 0.03 eV. The large amplitude and narrow width of this oscillator compared to those of typical electronic interband transitions in SiGe alloys indicates that the origin of this feature is not purely electronic. In an approximate way this enhancement can be plausibly explained by considering the NWs as microscale waveguide resonators [7]. In this reference it is shown that the absorption efficiency of Ge nanowires has distinctive peaks with energy positions and intensities that depend on nanowire size and light polarization. Those peaks, known as "leaky mode resonances" (LMR) appear when light is trapped by multiple total internal reflections within the nanowire, in general for subwavelength dimensions [19]. Following Ref. [7] we have calculated the LMR positions for normal-incidence illumination as a function of nanowire size. For this, we use the dielectric function of  $\text{Si}_{0.7}\text{Ge}_{0.3}$  alloy plotted in Fig. 5

and find the light wavelengths that satisfy the characteristic equation (Eq. (1) of Ref.[7]). The TM modes (with electric field along the NW axis) in Ge NWs give rise to enhanced optical absorption compared to the TE modes [7]. This calculation assumes a cylindrical geometry of the NWs which in our case is a rough approximation. The shape of the NWs is approximately elliptical if we disregard the existing facets. However, a calculation taking into account the full NW morphology is much more complicated and out of the scope of the present work. The calculated energies of LRM modes in cylindrical  $\text{Si}_{0.7}\text{Ge}_{0.3}$  NWs are plotted in the upper part of Fig. 5. We consider that the NW radius in our case is given by the geometric mean of the two main dimensions (width and height), i.e., a size range of 40–60 nm. The strong resonance observed at 2.54 eV could correspond to the main  $\text{TM}_{11}$  and  $\text{TM}_{21}$  LMR modes for NWs of 40 nm and 60 nm, respectively. The calculations also show that LMRs exist only in the spectral region where the SiGe alloy NWs are transparent or have low absorption. The resonances disappear above 3 eV with the strong absorption of the  $E_1$  and  $E_1 + \Delta_1$  transitions of  $\text{Si}_{0.7}\text{Ge}_{0.3}$ . In this calculation the substrate is not taken into account. However, the substrate does not affect much the energies of the LMRs [7] but it does affect the waveguiding effect. In this case, for the considered alloy composition, the energy at which the refractive index of Si becomes larger than that of the SiGe alloy which would prevent the multiple internal reflections necessary for the LMR is also about 3 eV. The data presented in Fig.5 suggest that the  $n$  and  $k$  values of the NWs are relatively similar to the bulk for light polarized perpendicular to the NW axis but quite different when the polarization is along it, and it is plausible to attribute this difference to the presence of waveguide-like leaky resonant modes in the NWs.

## 5 Conclusions

In this work, we characterized a thin film containing self-assembled  $\text{Si}_{1-x}\text{Ge}_x/\text{Si}$  in-plane nanowires grown by Molecular Beam Epitaxy on a Si (001) substrate. Individual nanowires could be studied within the spatial resolution of  $\sim 1\ \mu\text{m}$  using a Spectroscopic Imaging Ellipsometer offering improved sensitivity with respect to polarized optical microscopy. Measured  $\psi$  and  $\Delta$  maps of the imaged sample region allowed to identify both compositional inhomogeneity of the  $\text{Si}_{1-x}\text{Ge}_x$  material as well as strong in-plane anisotropy of the optical response of the nanowires. The measured SIE spectral behavior of  $\psi$  and  $\Delta$  in the different regions of the sample gave insight into both aspects. Spatial resolution was found to be essential to discern different contributions from the film regions that in principle are contained in an average SE spectrum. In the studied case, a large contribution arising from NWs oriented along the plane of incidence was absent in the general SE measurement. Therefore, the NW anisotropic behavior could only be studied when sufficient spatial resolution SIE measurements were performed. A plausible explanation of the observed anisotropy was the presence of waveguide-like leaky resonant modes in the NWs. The results show the unique potential of imaging ellipsometry to study micro- and nanostructured semiconductor samples.

## 6 Acknowledgments

We acknowledge funding by the Spanish Ministry of Economy and Competitiveness (MINECO) through grants CSD2010-00044 (Consolider NANOTHERM), MAT2013-47878-C2-1-R, MAT2015-70850-P, and the "Severo Ochoa"

Programme for Centres of Excellence in R&D (SEV-2015-0496).

## References

- [1] H. Fujiwara, *Spectroscopic Ellipsometry: Principles and Applications* (John Wiley & Sons, Chichester, UK, 2007).
- [2] M. Losurdo, M. Bergmair, G. Bruno, D. Cattelan, C. Cobet, A. de Martino, K. Fleischer, Z. Dohcevic-Mitrovic, N. Esser, M. Galliet, R. Gajic, D. Hemzal, K. Hingerl, J. Humlicek, R. Ossikovski, Z. V. Popovic, O. Saxl, Spectroscopic ellipsometry and polarimetry for materials and systems analysis at the nanometer scale: state-of-the-art, potential, and perspectives, *J. Nanopart. Res.*, 11 (2009), pp. 1521–1554.
- [3] A. Shan, M. Fried, G. Juhász, C. Major, O. Polgár, A. Németh, P. Petrik, L. R. Dahal, J. Chen, Z. Huang, N. J. Podraza, and R. W. Collins, High-speed imaging/mapping spectroscopic ellipsometry for in-line analysis of roll-to-roll thin-film photovoltaics, *IEEE Journal of Photovoltaics*, 4 (2014), pp. 355–361.
- [4] *Handbook of Ellipsometry*, edited by H. G. Tompkins and E. A. Irene (William Andrew Publishing, Norwich, NY, 2005).
- [5] M. Erman and J. B. Theeten, Spatially resolved ellipsometry, *J. Appl. Phys.*, 60 (1986), 859–873.
- [6] L. Asinovski, D. Beaglehole, and M. T. Clarkson, *Phys. Status Solidi A*, 205 (2008), pp. 764–771.
- [7] L. Cao, J. S. White, J.-S. Park, J. A. Schuller, B. M. Clemens, M. L. Brongersma, Engineering light absorption in semiconductor nanowire devices, *Nat. Mater.* 8 (2009) 643–647.



- [8] G. Brönstrup, N. Jahr, C. Leiterer, A. Csáki, W. Fritzsche, and S. Christiansen, Optical properties of individual Silicon nanowires for photonic devices, *ACS Nano* 4 (2010) 7113–7122.
- [9] M. I. Alonso, A. Ruiz, M. Alonso, E. Bailo, M. Garriga, A. Molero, P. O. Vaccaro, A. R. Goñi, Growth and characterization of epitaxial in-plane SiGe alloy nanowires, *Materials Today: Proceedings* 2 (2015) 548–556.
- [10] L. Yu, M. Xu, J. Xu, Z. Xue, Z. Fan, G. Picardi, F. Fortuna, J. Wang, J. Xu, Y. Shi, K. Chen, and P. Roca i Cabarrocas, In-plane epitaxial growth of Silicon nanowires and junction formation on Si(100) substrates, *Nano Lett.* 14 (2014) 6469–6474.
- [11] M. I. Alonso, E. Bailo, M. Garriga, A. Molero, P. O. Vaccaro, A. R. Goñi, A. Ruiz, M. Alonso, Composition and strain imaging of epitaxial in-plane SiGe alloy nanowires by micro-Raman spectroscopy, *J. Phys. Chem. C* 119 (2015) 22154–22163.
- [12] D. B. Murphy and M. W. Davidson, *Fundamentals of Light Microscopy and Electronic Imaging*, 2nd ed. (Wiley-Blackwell, Hoboken, NJ, 2013).
- [13] S. Funke, U. Wurstbauer, B. Miller, A. Matković, A. Green, A. Diebold, C. Röling, P. H. Thiesen, Spectroscopic imaging ellipsometry for automated search of flakes of mono- and n-layers of 2D-materials, *Appl. Surf. Sci.* this volume (2017) submitted.
- [14] M. I. Alonso, M. de la Calle, J. O. Ossó, M. Garriga, A. R. Goñi, Strain and composition profiles of self-assembled Ge/Si(001) islands, *J. Appl. Phys.* 98 (2005) 033530.
- [15] J. Humlíček, M. Garriga, M. I. Alonso, M. Cardona, Optical spectra of  $\text{Si}_x\text{Ge}_{1-x}$  alloys, *J. Appl. Phys.* 65 (1989) 2827–2832.

- [16] A. El Sachat, F. Alzina, J. S. Reparaz, C. M. Sotomayor-Torres, M. I. Alonso, M. Garriga, A. Ruiz, M. Alonso, P. O. Vaccaro, A. R. Goñi, Structure, composition and thermal properties of epitaxial  $\text{Si}_{1-x}\text{Ge}_x$  alloy nanowires, to be published.
- [17] E. D. Palik, *Handbook of Optical Constants of Solids*, vol. 1 (Academic Press, San Diego, 1985).
- [18] D. E. Aspnes, Approximate solution of ellipsometric equations for optically biaxial crystals, *J. Opt. Soc. Am.* 70 (1980) 1275–1277.
- [19] H.-S. Ee, J.-H. Kang, M. L. Brongersma, and M.-K. Seo, Shape-dependent light scattering properties of subwavelength Silicon nanoblocks, *Nano Lett.* 15 (2015) 1759–765.

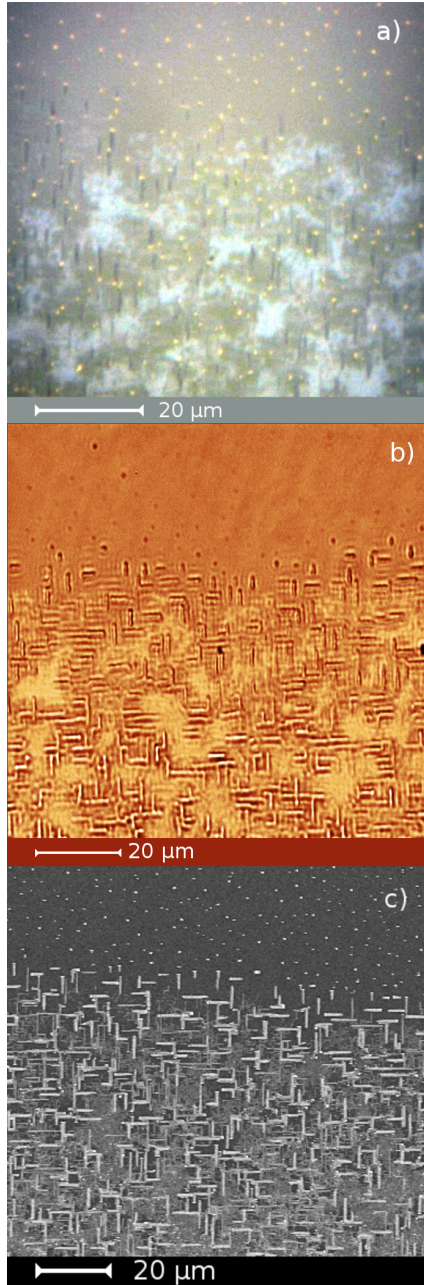


Fig. 1. Images of the studied film region. (a) Conventional optical micrograph with light polarized in the vertical direction. (b) Ellipsometric contrast micrograph recorded at 450 nm and  $40^\circ$  angle of incidence. Polarizer, compensator and analyzer angles were  $-40^\circ$ ,  $45^\circ$ , and  $65^\circ$  respectively. (c) Scanning electron micrograph. In all cases the upper parts of the images correspond to a sample region with AuSi seeds only. During deposition it was covered by a shadow mask to keep it as reference. The observed nanowires on the deposited region (lower part of the images) are along  $\langle 110 \rangle$ .

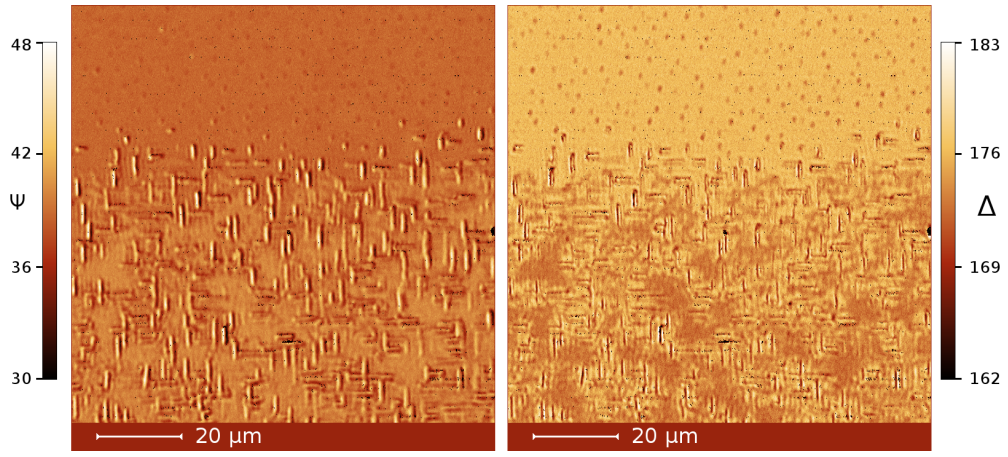


Fig. 2. Ellipsometric  $\psi$  and  $\Delta$  maps measured at 430 nm and  $40^\circ$  incidence, with plane of incidence projection along the vertical direction.

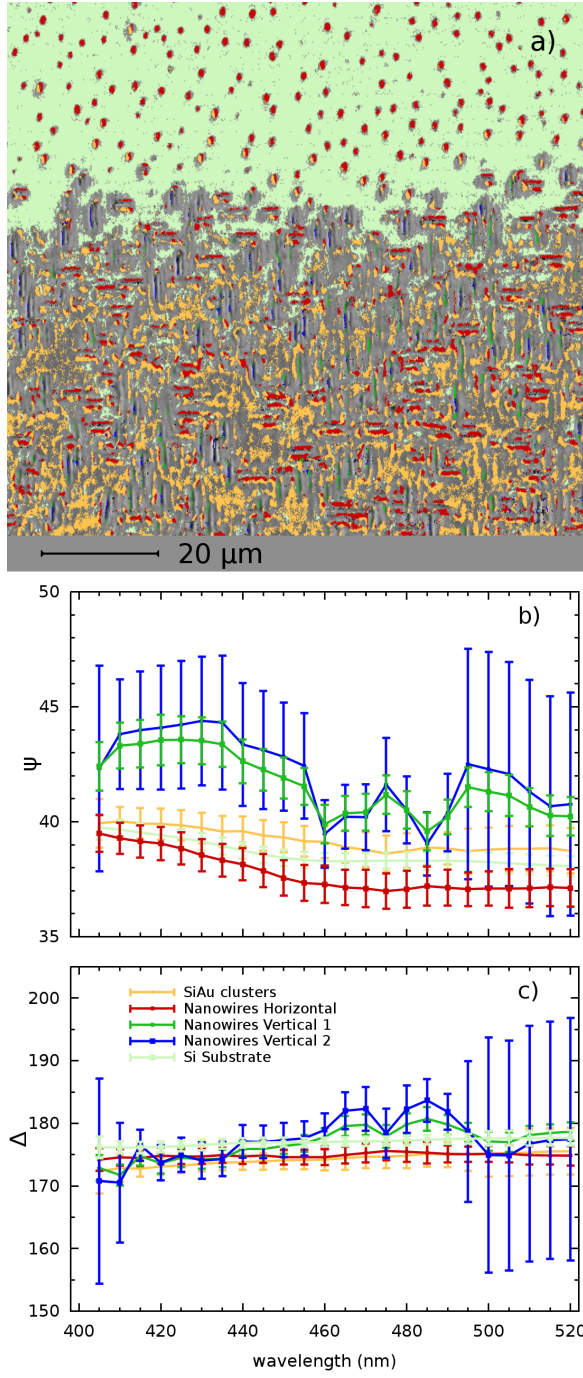


Fig. 3. Results of the flake search procedure on the SIE spectra. (a) Several identified regions of the film with similar optical properties within given bounds. (b) Corresponding average  $\psi$  and (c)  $\Delta$  spectra.

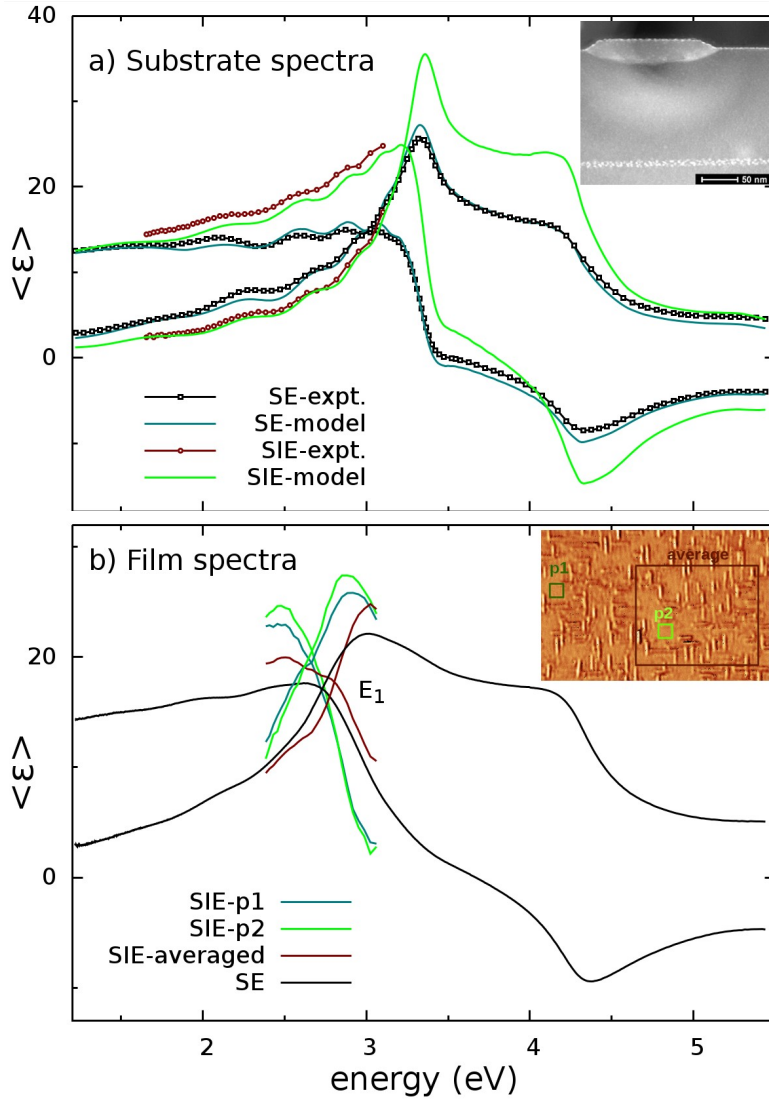


Fig. 4. Ellipsometric spectra of different regions of the film plotted as pseudodielectric functions. (a) Measurements on the substrate region (symbols) compared to the model discussed in the text (lines). The inset shows a cross section STEM image. (b) Measurements on the deposited region. p1 and p2 correspond to two different small regions on the coalesced film part, as depicted in the inset. The SIE-averaged spectrum considers the larger region including many features, and is more comparable to the SE spectrum.

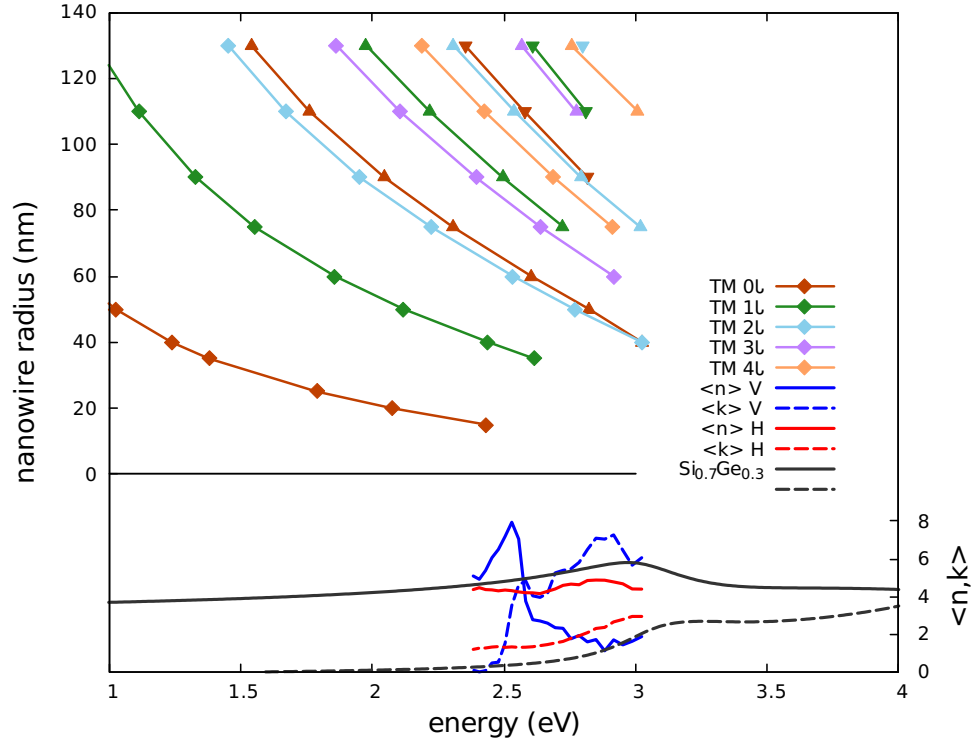


Fig. 5. Upper part: Energies of  $TM_{ml}$  waveguide leaky resonant modes calculated for a cylindric geometry for different nanowire radii (left y-axis). The  $n$  and  $k$  values considered for the calculation correspond to a Ge content of  $x=0.30$ , plotted in the lower part (right y-axis). The pseudo-values of  $n$  and  $k$  obtained along (V) or across (H) representative single NWs are also displayed.